Available online at www.sciencedirect.com

SciVerse ScienceDirect

Ceramics International 39 (2013) 529–538

CERAMICS INTERNATIONAL

www.elsevier.com/locate/ceramint

Characterization of $La_{0.58}Sr_{0.4}Co_{0.2}Fe_{0.8}O_{3-\delta}$–$Ce_{0.8}Gd_{0.2}O_2$ composite cathode for intermediate temperature solid oxide fuel cells

Na Li[a,*], Atul Verma[a], Prabhakar Singh[a], Jeong-Ho Kim[b]

[a]Center of Clean Energy Engineering, University of Connecticut, 44 Weaver Road, Unit 5233, Storrs, CT 06269, USA
[b]Department of Civil and Environmental Engineering, University of Connecticut, 261 Glenbrook Road, Storrs, CT 06269-2037, USA

Received 12 April 2012; received in revised form 18 June 2012; accepted 19 June 2012
Available online 26 June 2012

Abstract

$La_{0.58}Sr_{0.4}Co_{0.2}Fe_{0.8}O_{3-\delta}$–$Ce_{0.8}Gd_{0.2}O_2$ (LSCF–GDC) composite cathodes with various weight ratios 90%, 70% and 50% of LSCF were prepared. Mechanical properties, thermal expansion properties and electrical properties were measured for potential applications in solid oxide fuel cells (SOFCs) with graded cathodes. LSCF and GDC as pure cathode and electrolyte materials were characterized as reference. The absence of new phases as confirmed by X-ray diffraction (XRD) analysis demonstrated the excellent compatibility between the cathode and electrolyte materials. Mechanical properties such as hardness and fracture toughness were measured by the micro-indentation technique, while hardness and elastic modulus were measured by the nano-indentation technique. Thermal expansion behavior was recorded by a dilatometer. Electrical conductivity was measured by the four probe DC method. The 50% LSCF–GDC composite has the lowest relative density among all the samples. Thermal expansion coefficients (TECs) and electrical conductivity increased with addition of LSCF contents in the composite, while mechanical properties depended more on the density than the LSCF content.

Keywords: B. Composites; C. Electrical conductivity; C. Thermal expansion; E. Fuel cells

1. Introduction

Intermediate temperature (IT, 500–800 °C) SOFC has gained a considerable attraction compared to a traditional high-temperature SOFC in that the reduced operation temperature allows low-cost metallic interconnects [1], helps to avoid material compatibility challenges at high temperature [2], reduces sealing and thermal degradation problems [3], and eventually accelerates the commercialization of SOFC technology. The overall cell performance, however, tends to decrease because of the reduced ionic conductivity of electrolyte and the increased polarization resistance of electrodes, especially on the cathode side [1]. Thus the development of higher-performance cathode is critical to overcome such technical barriers.

LSCF is one of the promising cathode materials for SOFC operated below 800 °C. Impedance spectroscopy data for LSCF electrodes have shown lower interfacial resistance than do conventional LSM electrodes [3]. The electrical conductivity of certain perovskite composition $La_{0.6}Sr_{0.4}Co_{0.2}Fe_{0.8}O_3$ can exceed 300 S/cm [4,5]. This composition is also attractive because the high Fe content yields a low thermal expansion coefficient than those of low Fe compositions, better matching the low TEC of the electrolyte. Unfortunately, LSCF cannot be used in conventional SOFCs because the LSCF perovskites are chemically incompatible with the YSZ electrolyte [6]. Fe or Co based cathode materials react readily with YSZ, forming high resistance phases $La_2Zr_2O_7$ and $SrZrO_3$ at the interface at high temperatures that deteriorate the cell performance [7,8]. The materials chemically compatible with Co-containing cathodes are doped ceria electrolytes, which possess a higher ionic conductivity than that of YSZ [9].

A commonly used method for improving the cathode performance is to add an ionically conducting second

*Corresponding author: Tel.: +1 860 486 5668; fax: +1 860 486 8378.
E-mail addresses: nali@engr.uconn.edu, bluegrape2008@gmail.com (N. Li).

0272-8842/$36.00 © 2012 Elsevier Ltd and Techna Group S.r.l. All rights reserved.
http://dx.doi.org/10.1016/j.ceramint.2012.06.059

phase [10,11]. In the present work, $Ce_{0.8}Gd_{0.2}O_2$ was added to $La_{0.58}Sr_{0.4}Co_{0.2}Fe_{0.8}O_{3-\delta}$ to form a mixed conducting cathode of LSCF–GDC. The concept of functionally graded materials (FGMs) is also used to enhance the mechanical durability of the LSCF–GDC composite. The cathode in this study is designed with four layers consisting of 100% LSCF, 90% LSCF, 70% LSCF and 50% LSCF adjacent to the electrolyte GDC layer. General perspectives of material gradation have been described by Sasaki and Gauckler [12]. Instead of an abrupt change in composition and/or microstructure between the two materials, FGMs have a graded interface at which the composition gradually changes from one material to the other [13]. The difference with respect to physical properties of the cathode and electrolyte such as sharp discontinuities in TECs, which could result in delamination during thermal cycling, may be enhanced by allowing a gradual change in the composition between the two materials [14,15].

The objective of this study is to provide material properties of a graded LSCF–GDC cathode with various volume fractions of LSCF and GDC as materials database. The data for a dense cathode produced herein can be modified for the effective medium with realistic cathode porosities in an actual SOFC. In this regard, the present material properties can be the basis for predicting the thermo-mechanical behavior of the graded SOFC cell in operation environment (e.g. using finite element methods) which in general possesses enhanced mechanical durability (with lower probability of failure) and material compatibility compared to a typical layered SOFC.

The graded cathode is designed with four layers consisting of different LSCF contents adjacent to the electrolyte GDC layer. The LSCF–GDC pellets with four different compositions (100%, 90%, 70% and 50% LSCF) were prepared and characterized as each layer of the graded cathode. The electrical conductivity, thermal expansion and mechanical properties were measured with respect to the sintering temperature and the LSCF content.

2. Experiment

$La_{0.58}Sr_{0.4}Co_{0.2}Fe_{0.8}O_x$ with a specific area 12.2 m^2/g was purchased from Seimi Chemical Corporation, and $Ce_{0.8}Gd_{0.2}O_2$ with a specific area 11.4 m^2/g was purchased from Daiichi Kigenso Kagaku Kogyo Corporation (DKKK) in Japan. LSCF–GDC cathode powders were prepared by ball milling LSCF and GDC powders for 24 h in ethanol to achieve good mixing. The weight percentage of LSCF in the mixing powders is 100%, 90%, 70%, 50% and 0%. After ball milling, the wet slurries were dried at 80 °C; then the dried powders were ground with a mortar and pestle and passed through 100 mesh sieves. The specific surface area of each powder after ball milling was determined through nitrogen adsorption based on the Brunauer–Emmett–Teller (BET) method [16] using a gas sorption analyzer (Nova 1000). The measured specific surface area was used to evaluate the properties of starting powders.

Monolithic pellets and rectangular bars were obtained by uniaxial pressing at 100 MPa and then sintered in air for 2 h with a heating rate of 2 °C/min. 100% LSCF samples were sintered at 1200 °C, 100% GDC samples were sintered at 1400 °C, and the composite samples were sintered at 1000, 1100 and 1200 °C. Phase characterization was determined by XRD analysis using Cu Kα radiation (Bruker D5005 advance X-ray diffractometer). The bulk density was determined by the Archimedes method with deionized water as the immersing medium. Basically specimens were saturated by boiling for 2 h and then cooling to room temperature. Then the wet weight (M_3), float weight (M_2) and dry weight (M_1) were recorded. The bulk density (D_b) was calculated using

$$D_b = \frac{M_1 D_1}{M_3 - M_2}, \tag{1}$$

where D_1 is the density of the distilled water. Theoretical density of pure LSCF and GDC was calculated using the lattice parameters obtained from XRD analysis. Theoretical density of LSCF–GDC composites was calculated by the rule of mixture [17]; the simplest mathematical expression for rule of mixture for a binary solid solution A–B is

$$a = a_A(1-x) + a_B x \tag{2}$$

in which a is the property, x is the mole fraction of component B, and $(1-x)$ is the mole fraction of component A.

The sintered bars were about $3 \times 4 \times 50\ mm^3$ in dimension; pellets were about 10 mm in diameter and 2 mm in thickness. Rectangular samples were used for thermal expansion tests and electrical conductivity tests. Thermal expansion properties were measured using a Netzsch 402PC dilatometer in air over a range from the room temperature to 1000 °C with a heating rate 3 °C/min. A standard alumina rod was used for calibration. The average TEC was calculated from the expansion curve using

$$\alpha = \frac{1}{L_0}\frac{\Delta L}{\Delta T} \tag{3}$$

where L_0 is the initial length of the sample, ΔL is the sample length change and ΔT is the range of temperature variation.

Electrical conductivities were measured using the standard DC four probe technique with a Keithley 2440 sourcemeter in a tube furnace in air upon cooling from 800 °C to 200 °C. Two inner platinum wires acted as current contacts and the other outer two wires acted as the voltage contacts. They were attached to the rectangular bars by painting platinum paste along the circumference. A constant current was applied to the current wires and the voltage response on the voltage wires was recorded. The conductivity was determined from a set of I–V values by taking

$$\sigma = \frac{L}{A}\frac{dI}{dV} \tag{4}$$

where L is the length, A is the area, I is the current and V is the voltage. The measurements were performed at low V and I values to ensure the validity of Ohm's law.

The samples need to be mounted and polished before indentation tests. The pellets were mounted using a Buehler epo-thin low viscosity epoxy resin and a hardener, and cured overnight at room temperature. Then the mounted samples were ground by sand paper step by step from 180, 320, 400, 600 to 1200 grit and finally polished down to 1 μm by diamond slurry.

Vickers micro-hardness tests were done by using a Leco DM-400 FT hardness tester with 300 g load held for 15 s. At least 10 micro indents were made for each sample. The diagonal lengths of the indents (d_1 and d_2) were measured using an objective lens of 60× and the corresponding Vickers hardness (H_v) was directly reported. The Vickers hardness was calculated by

$$H_v = \frac{2P\sin(\theta/2)}{d_1 d_2} \quad (5)$$

in which P is load and $\theta = 136^\circ$. Indentations were made in different areas and with at least 50 μm distance between two indents to make the data more representative.

The indents after micro-hardness tests were studied using scanning electron microscopy (SEM , JEOL JSM-5600LV). The average length of cracks propagated from the indents tips after micro-hardness tests were measured to calculate the fracture toughness (K_c) using the formula

$$K_C = 0.016(E/H)^{1/2}(P/C^{3/2}) \quad (6)$$

where P is the load, H is the hardness, E is the elastic modulus and C is the half-crack size.

Nano-indentation tests were done using an MTS Nano Indenter XP. A Berkovich indenter was used for nano-indentation testing. The Berkovich hardness (H) and the elastic modulus (E) were calculated by software Testwork 4. The mean contact pressure is usually determined from a measure of the plastic depth of penetration

$$A = 3\sqrt{3}h_p^2 \tan^2\theta \quad (7)$$

where $\theta = 65.27^\circ$ for the Berkovich indenter; hence the mean contact pressure, or hardness, is

$$H_B = \frac{P}{24.5h_p^2} \quad (8)$$

All pellets were tested at room temperature with 50 g applied load held for 30 s. All the data were recalculated using frame stiffness 3.9×10^6. The elastic modulus was calculated according to the equation

$$\frac{1}{E_r} = \frac{1-v_{indentor}^2}{E_{indentor}} + \frac{1-v_{sample}^2}{E_{sample}} \quad (9)$$

where $v_{indenter}$ and v_{sample} are the Poisson ratios, whereas $E_{indenter}$ and E_{sample} are the elastic modulus of the diamond indenter and the sample, respectively [18]. The elastic modulus of the sample was calculated using $v_{indenter} = 0.07$ and $E_{indenter} = 1140$ Pa for the diamond indenter and assuming $v_{sample} = 0.3$ from literature [19].

3. Results and discussion

3.1. XRD analysis

Fig.1(a) shows XRD patterns of the 50% LSCF–GDC composite sintered at 1000 °C, 1100 °C and 1200 °C for 2 h, while Fig.1(b) shows XRD patterns of the composite sintered at 1200 °C with 50%, 70% and 90% LSCF contents. The pure LSCF and GDC samples were used as references. LSCF shows the perovskite cubic structure and GDC shows the fluorite structure, and no second phase was detected in the composites. This means that there are no chemical reactions between LSCF and GDC during the sintering process. LSCF and GDC are chemical compatible up to 1200 °C at different mixing ratios. The LSCF–GDC composite can be chosen as cathode materials and would not react with GDC electrolyte or interlayers.

3.2. Density

Theoretical densities were calculated to be 6.35 g/cm^3 for LSCF and 7.31 g/cm^3 for GDC from XRD analysis.

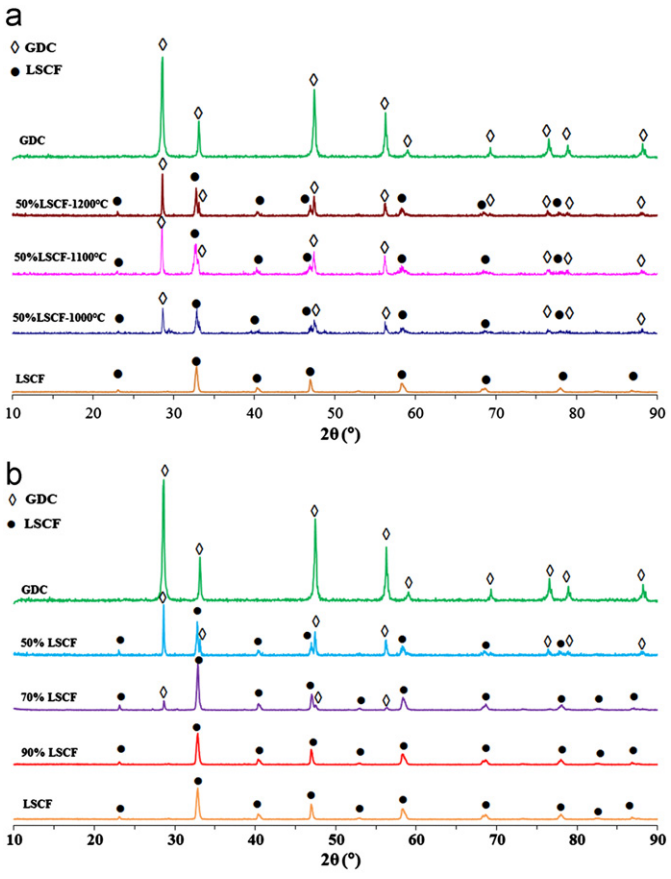

Fig. 1. (a) XRD patterns of 50 wt% LSCF–GDC composite sintered at 1000, 1100 and 1200 °C and (b) XRD patterns of LSCF–GDC composite sintered at 1200 °C with different LSCF contents.

Theoretical densities of the composite were calculated using the rule of mixture. Bulk density was measured from the Archimedes method, and relative density was defined as the ratio of bulk density to theoretical density. Fig. 2 shows the density of LSCF–GDC pellets pressed at the same pressure and sintered at the same temperature. With the addition of LSCF content, the bulk density tends to decrease, but not in a linear way. All samples have densities greater than 94% of theoretical densities. It is also observed that 50 wt% composition LSCF has the lowest relative density. This result is consistent with R.A. Cutler's observation that the end components sintered more readily than the composites [17].

3.3. Surface area and microstructure

The surface areas of the LSCF–GDC powder after mixing were determined using the BET principle and are shown in Table 1. The measured surface areas of all the raw and developed powders are in the range of 11–14 $m^2 g^{-1}$. The close surface area value indicates that the ball milling process did not change the particle size much. The particle size effect on the sintering and properties may be neglected during discussion.

The SEM images of the fracture surface for GDC, LSCF and 50% LSCF–GDC samples are shown in Fig. 3(a)–(c), respectively. All the samples showed brittle fracture with mixed transgranular and inter-granular fracture mechanism. The 50% LSCF–GDC composite shows a porous matrix and has higher porosity than those of LSCF and GDC samples, which is in agreement with the density measurement. Thermal etching was conducted on the polished surface to expose grain boundaries and the microstructure is shown in Fig.3(d)–(f). GDC has coarse grain about 0.7 μm and LSCF has fine grain about 0.5 μm. However, both phases (bright phase is GDC, and dark phase is LSCF in Fig. 3(f)) show smaller grains of 0.3 μm in the composite sample.

3.4. Mechanical properties

Fig. 4 shows typical micro- and nano-indents observed in SEM. The four-sided micro-indents are around 22 μm in diagonal length. The triangular nano-indents are around 6 μm in the side. The pyramid shape of the Berkovich indenter provides a sharper point than the four-sided Vickers geometry, therefore ensuring a more precise control over the indentation process. Reproducible hardness and fracture toughness were obtained through micro-indents; reproducible hardness and elastic modulus were obtained from nano-indents.

Fig. 5 shows the load–displacement curves of nano indentation tests. The loading–unloading curve shows typical behavior for ceramics materials. There is no pop-in formation that would indicate large inhomogeneities in the material [20]. Upon the same loading, a larger penetration depth means the material matrix is weaker and deforms more. The initial slope of unloading segment was used to calculate the elastic modulus. The steeper the unloading curve, the larger the elastic modulus. We could

Table 1
Specific surface area of the powders measured by the BET method.

Powder	Specific surface area (m^2/g)
LSCF	12.4
90% LSCF–GDC	11.8
70% LSCF–GDC	14.2
50% LSCF–GDC	13.2
GDC	11.3

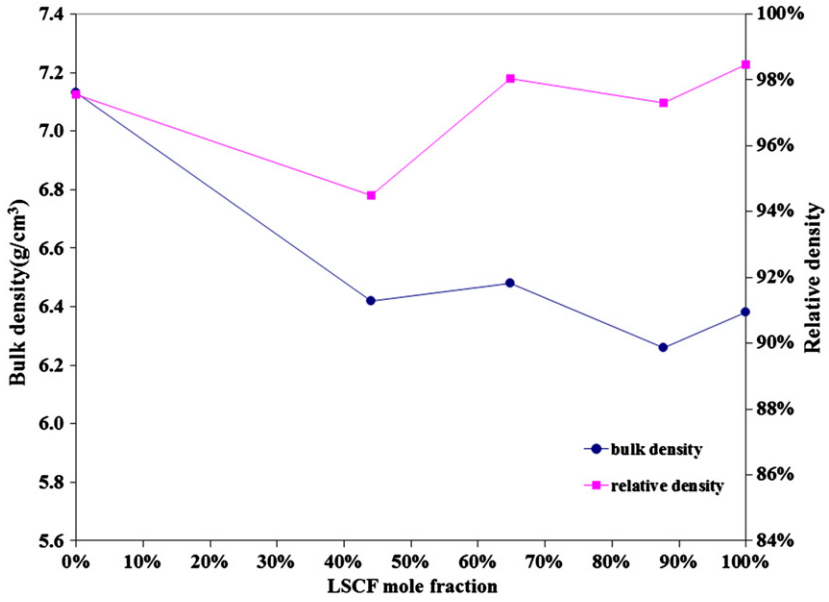

Fig.2. Density of the sintered GDC, LSCF and LSCF–GDC composites.

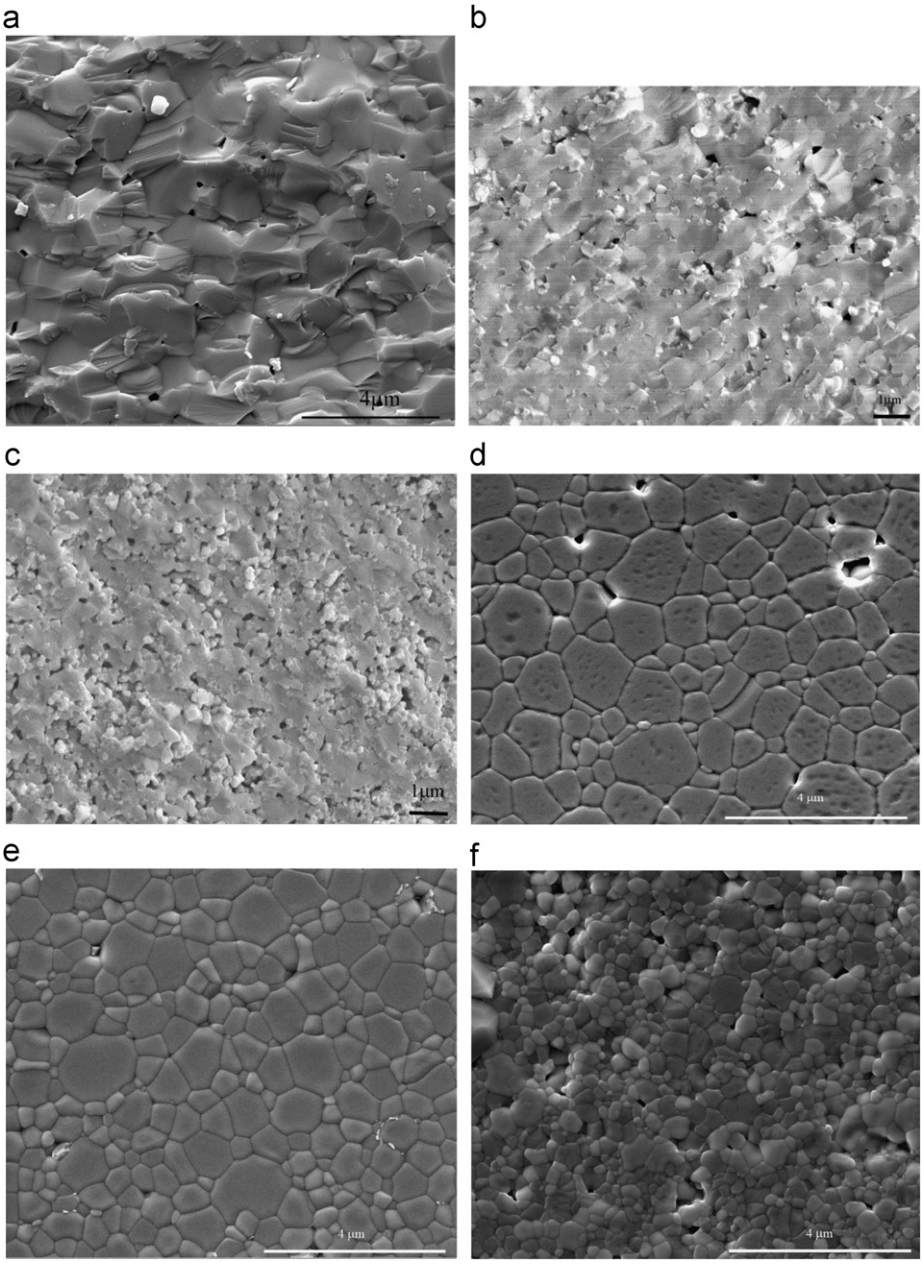

Fig.3. SEM image of fracture surface for the sintered samples: (a) GDC, (b) LSCF, (c) 50% LSCF–GDC; SEM image of the thermal etched samples (d) GDC, (e) LSCF and (f) 50% LSCF–GDC.

see that the 50% LSCF sample has the largest displacement and the smallest unloading slope, and then 90% LSCF, 100% LSCF, 70% LSCF and 100% GDC, but these four plots are very close. So the mechanical property of these four compositions calculated from the loading–unloading curves will be close and does not change significantly with the considered compositions.

In this work, hardness and elastic modulus of LSCF–GDC composites were characterized by depth-sensing indentation tests to explore the porosity and composition effect on the measured properties. By varying the peak load, moreover, the variation of the properties with the penetration depth was evaluated. Hardness and elastic modulus of the LSCF are shown in Fig. 6 as a function of peak load. It can be observed that the hardness and the elastic modulus do show the evidence of indentation size effect clearly [21]. At different peak loads, we get different hardness and elastic modulus values. The values decreased with the peak loads and became stable after 250 mN. At lower peak loads, the standard deviation is larger. At higher load, the standard deviation becomes smaller. For an example, at a peak load of 30 mN the percentage

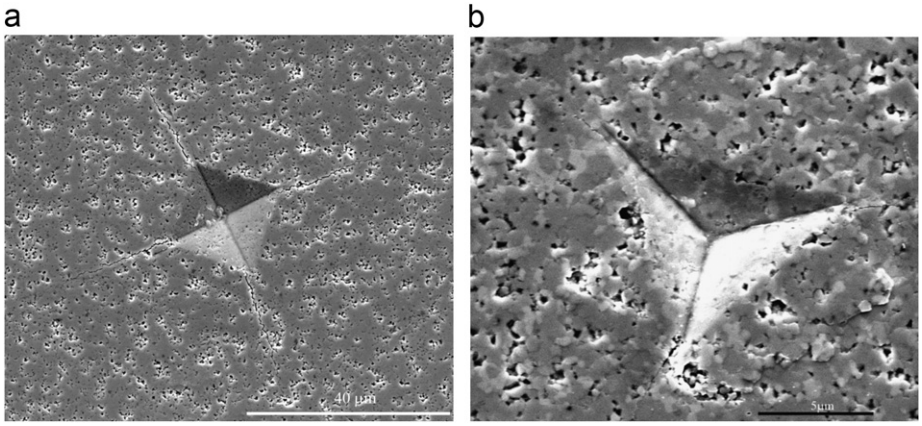

Fig.4. SEM image of (a) micro-indents of LSCF sample sintered at 1200 °C and (b) nano-indents of 70% LSCF–GDC sample sintered at 1200 °C.

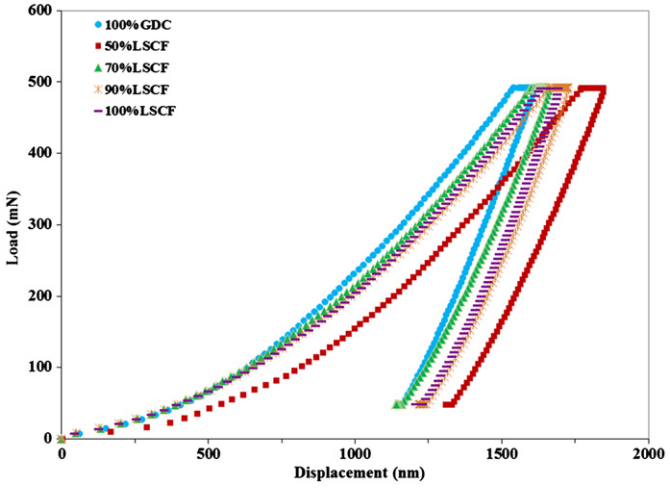

Fig.5. Nano-indentation load–displacement curves for LSCF–GDC composite with different LSCF content.

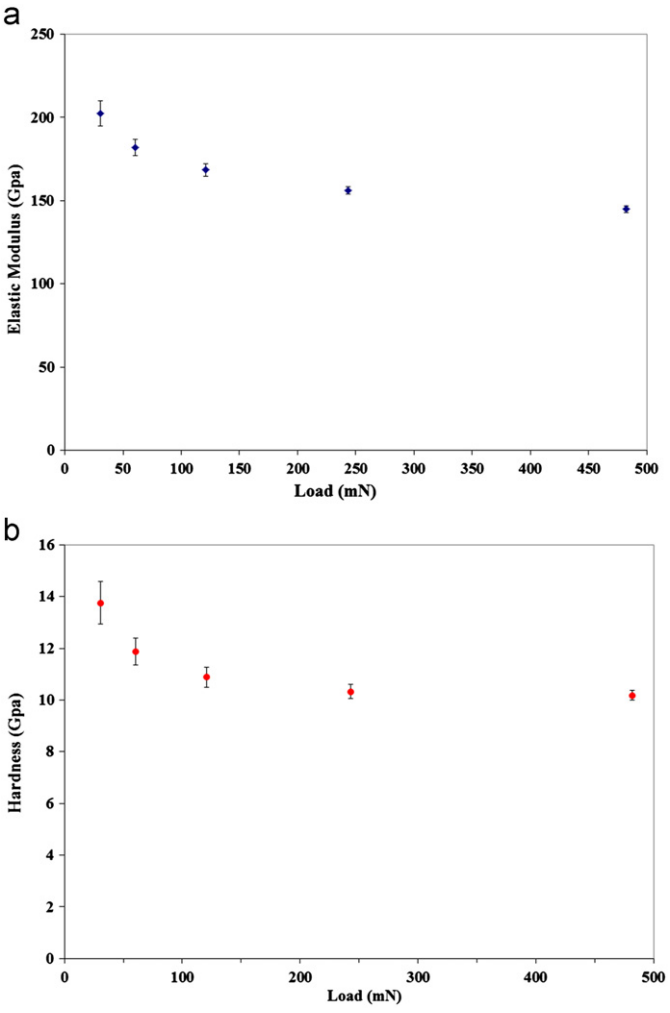

Fig.6. Indentation size effect of 70% LSCF–GDC sample sintered at 1200°C: (a) Elastic modulus indentation size effect and (b) hardness indentation size effect.

difference between the highest and the lowest value of elastic modulus was about 14.7%. At a peak load of 490 mN, this difference was only about 5.6%. For the reported data in this study, all samples were tested at the maximum load 490 mN to minimize the indentation size effect.

The calculated elastic modulus, hardness and fracture toughness data are shown in Fig.7. The range of hardness, elastic modulus and fracture toughness values is in good agreement with results previously reported in literature [19,22]. Furthermore, Fig. 7(a) shows that the elastic modulus is related with LSCF mole content. A similar trend is present for the relative density as a function of LSCF mole content. The identical LSCF content dependence of both modulus and densities implies that the two factors are probably linearly related to each other [23]. This inference is found to be true as shown in Fig. 8(a); the modulus and density result is successfully fitted by a linear law. D. Music studied the relation between modulus and density of boron suboxide, and fitted the data well using a linear or power law [24,25]. The elastic modulus relates to density because elastic modulus is insensitive to flaw size and is a measure of bonding at an atomic level, but porosity lowers the elastic modulus of ceramic materials [17].

Fig. 7(b) shows that micro-hardness is lower than nano-hardness, which can be explained as the micro-indenter has

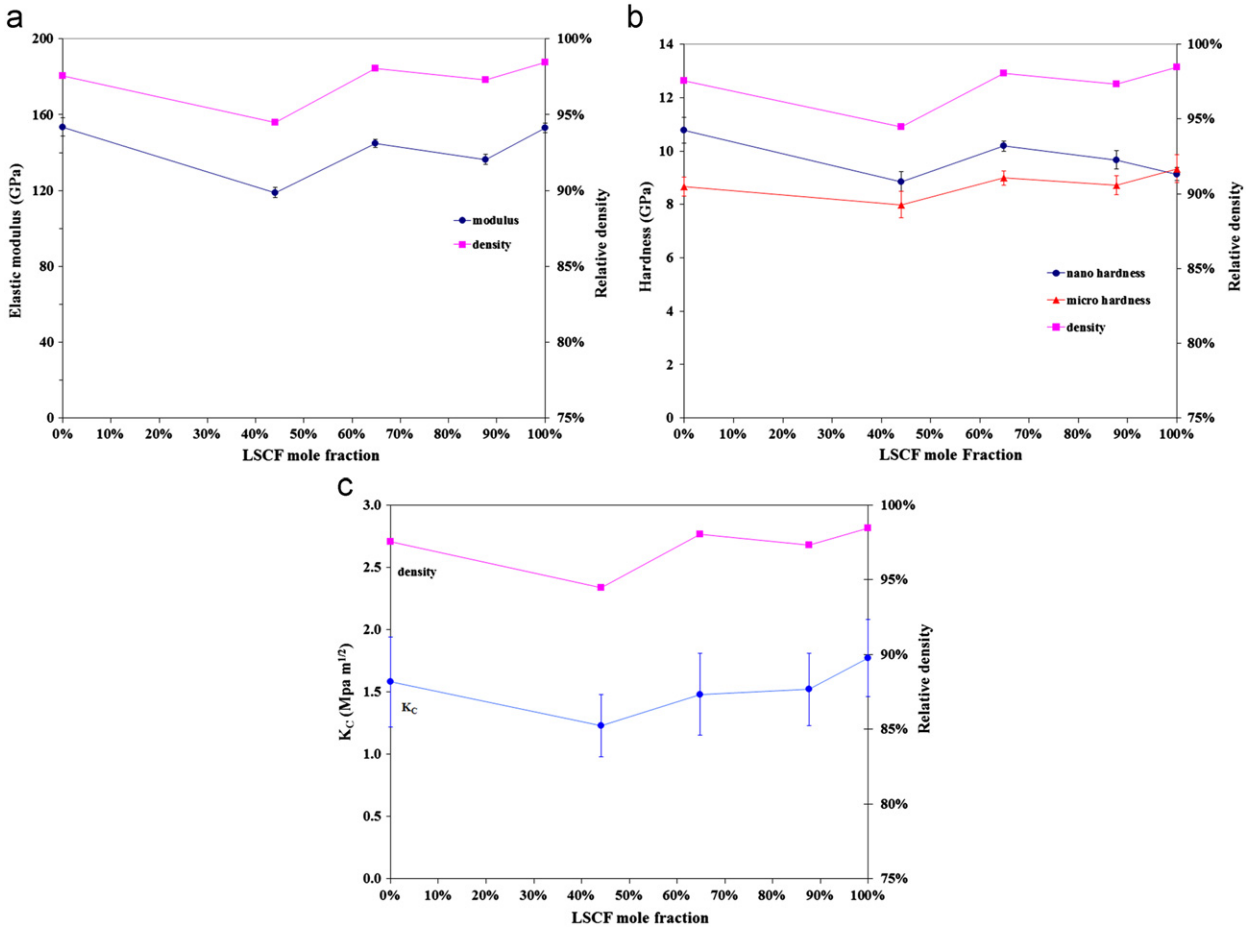

Fig. 7. (a) Elastic modulus and the relative density of LSCF–GDC composite as a function of LSCF mole content. (b) Micro- and nano- hardness and the relative density of LSCF–GDC composite as a function of LSCF mole content. (c) Fracture toughness and the relative density of LSCF–GDC composite as a function of LSCF mole content.

a larger contact area than the nano-indenter so it has more chance to be exposed to defects and pores. Both the micro- and nano-hardness are linearly related to the change in density as shown in Fig. 8(b). Kim and Khalil [26] and Chen et al. [27] studied the relationship of sintering density and hardness of ceramic materials, and reported that hardness increased with the increase of density. Besides elastic modulus and hardness, fracture toughness is also linearly related to the relative density as shown in Figs. 7(c) and 8(a).

The mechanical properties of a composite depend on the composition as well as density. As shown in Fig. 7, samples of LSCF and GDC in this study showed similar modulus, hardness and fracture toughness values. Each component almost contributed equally to the mechanical properties of the composite according to the rule of mixture, so the value of the composite depends more on density rather than composition.

3.5. Thermal expansion analysis

The linear thermal expansions of LSCF–GDC cathode with 0, 50, 70, 90, and 100 wt% LSCF are shown in Fig. 9(a) as a function of temperature. The TEC values of LSCF–GDC were calculated according to the linear thermal expansion curves and are given in Table 2 from room temperature to 700 °C and to 1000 °C. Among these samples the expansion is found to be the lowest for GDC, and the highest for LSCF. The composites have closer thermal expansion curves to one another. The slope for the LSCF–GDC samples increases with increasing LSCF content. It can be concluded that TEC increases with the increase of the LSCF content. Also, the slope of thermal expansion curves shows gradual increase in the high temperature region, which can be explained by the loss of oxygen at elevated temperature [28]. It has been reported that the thermal expansion curves deviate from straight lines for LSCF [28] and PSCFS systems [29].

Matching TECs in the SOFC components is critical, as small difference in the TEC of the cell components can produce large thermal stresses during single cell fabrication and fuel cell operation. Multilayered cathodes with graded composition of LSCF and GDC can reduce the mismatch between GDC electrolyte and LSCF cathode, decrease interfacial stress and increase the durability of fuel cells in operation.

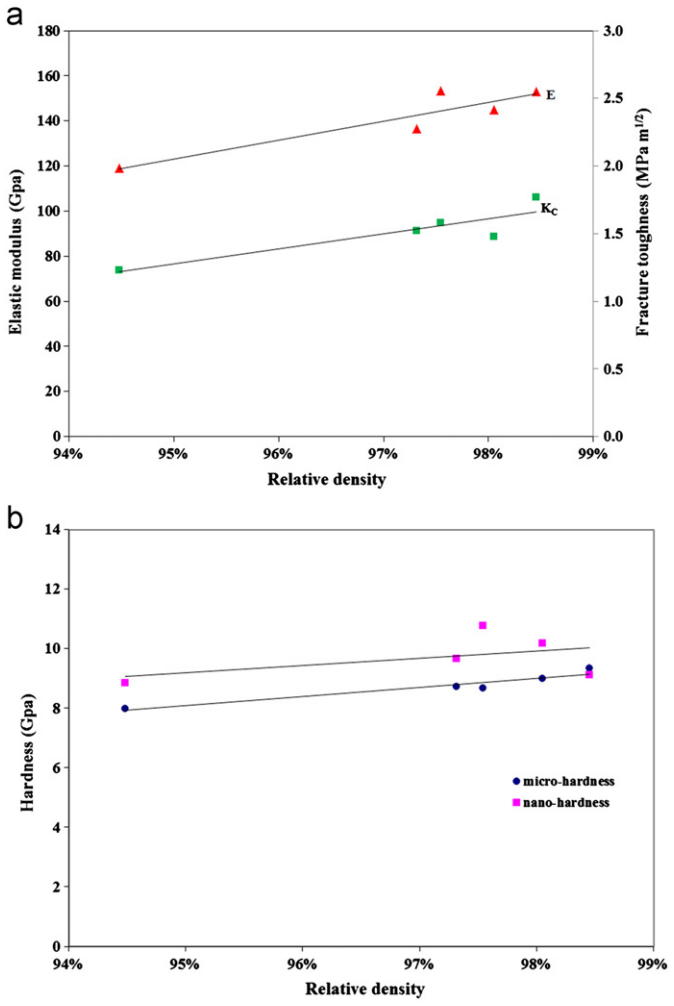

Fig. 8. (a) Elastic modulus and fracture toughness as a function of relative density. (b) Micro- and nano-hardness as a function of relative density.

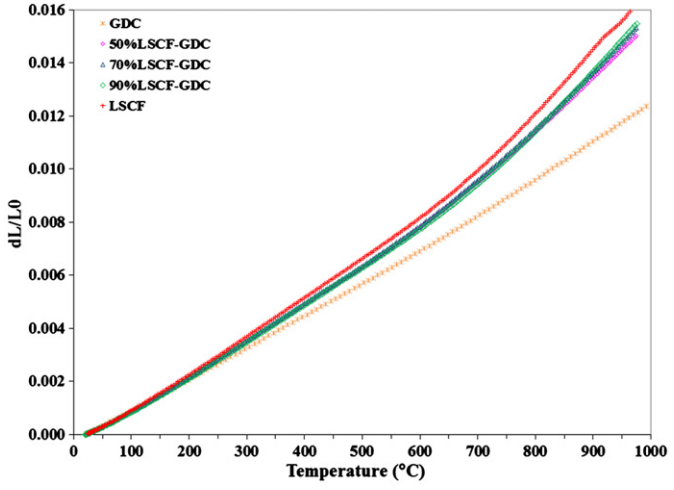

Fig.9. Linear thermal expansion curves of LSCF–GDC composite with different LSCF contents.

3.6. Electrical conductivity

Fig.10 shows $\log(\sigma T)$ of LSCF and LSCF–GDC as a function of reciprocal temperature. Clearly, the $\log(\sigma T)$ curve has good linear dependence of reciprocal temperature before 700°C, which is consistent with the small polaron conduction mechanism:

$$\sigma = \frac{c}{T}\exp\left(-\frac{E_a}{k_B T}\right), \tag{10}$$

where c is a constant, E_a is the activation energy, k is the Boltzmann constant, and T is the absolute temperature. The measured conductivity of pure LSCF was as high as 366 S/cm. With the addition of GDC content, the conductivity decreased accordingly. The electrical conductivity of all compounds increased with temperature up to about 700 °C. At higher temperatures a steep conductivity decrease was observed. The conductivity decrease above 600 °C is attributed to the loss of lattice oxygen [4,18,28].

All the samples sintered at 1200 °C for 2 h were measured for density, TECs and conductivity; the experimental data was summarized in Table 2. The results are comparable to those in literature [6,30–35].

4. Conclusions

LSCF–GDC composites with different compositions were prepared and the relative density of 94–98% was achieved after sintering at 1200 °C for 2 h. XRD analysis showed no chemical reaction between two phases up to 1200 °C sintering temperature. Thermal expansion behavior, electrical conductivity and mechanical properties were examined and supplied as a material database. Thermal expansion coefficient was in the range $12.3–15.5\times10^{-6}$ °C from room temperature to 800 °C. Electrical conductivity was from 140 to 366 S/cm at 600 °C. TECs and electrical conductivity increased with addition of LSCF contents in the composites. Elastic modulus was 119–153 GPa, nano-hardness 8.9–10.8 GPa, micro-hardness 8.1–9.8 GPa, and Fracture toughness 1.2–1.8 $Mpam^{1/2}$. The 50% LSCF–GDC composite has the lowest relative density in all the samples. TECs and electrical conductivity increased with addition of LSCF contents in the composites, while hardness, elastic modulus and fracture toughness linearly related to the relative density other than composition.

The properties of each layer of the graded cathode were characterized and used in the mechanical modeling. It can also be used to compare the LSCF–GDC composite cathode. Based on the present work, all the composite cathodes have similar mechanical properties. For comparison, 50% LSCF cathode has low conductivity, while 70% LSCF and 90% LSCF have similar TECs, but 90% LSCF has higher conductivity. If only one layer cathode is designed, 90% LSCF would be the best choice to be a cathode material considering the TEC, electrical conductivity and mechanical properties.

Table 2
Density, electrical conductivity and thermal expansion data for LSCF–GDC samples.

LSCF weight content (%)	LSCF molar content (%)	Bulk density (g/cm^3)	Theoretical density (g/cm^3)	Relative density (%)	TEC ($K^{-1}/10^{-6}$) at 20 °C ($K^{-1}/10^{-6}$)		Conductivity (S/cm)	
					700 °C	1000 °C	600 °C	800 °C
0	0.0	7.13	7.31	97.5	12.0	12.7	–	–
50	44.1	6.42	6.79	94.5	13.9	15.7	140	112
70	64.8	6.48	6.61	98.0	14.1	16.1	251	205
90	87.7	6.26	6.43	97.3	13.9	16.2	324	271
100	100.0	6.25	6.35	98.5	14.6	16.9	366	314

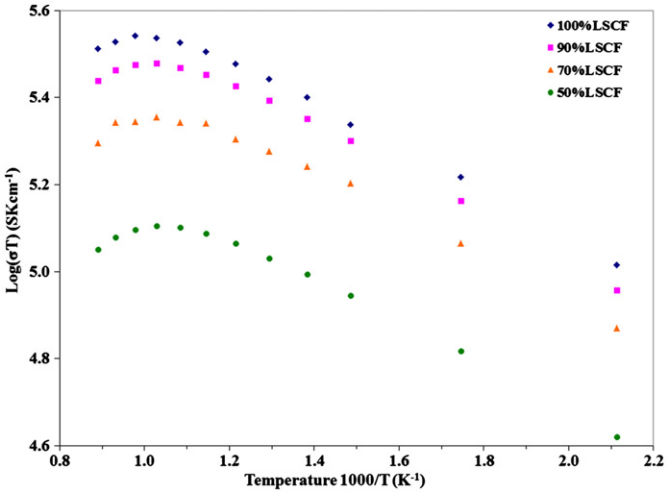

Fig.10. Conductivity of LSCF–GDC composites cathode with different LSCF content.

Acknowledgment

JHK gratefully acknowledges the financial support from the National Science Foundation (NSF) under the Faculty Early Career Development (CAREER) Grant CMMI-0546225 (Material Design and Surface Engineering Program). The authors would also like to acknowledge the technical support from the C2E2 (Center for Clean Energy Engineering) and the IMS (Institute of Materials Science) for their experimental program. Also appreciated is the technical assistance of Prof. Rainer Hebert and his graduate student Ms. Girija Marathe in nano-indentation experiments. Any opinions expressed herein are those of the writers and do not necessarily reflect the views of the sponsors.

References

[1] S.P. Jiang, W. Wang, Fabrication and performance of GDC-impregnated (La,Sr)MnO_3 cathodes for intermediate temperature solid oxide fuel cells, Journal of the Electrochemical Society 152 (2005) A1398–A1408.

[2] Z. Duan, M. Yang, A. Yan, Z. Hou, Y. Dong, Y. Chong, M. Cheng, W. Yang, $Ba_{0.5}Sr_{0.5}Co_{0.8}Fe_{0.2}O_{3-\delta}$ as a cathode for IT-SOFCs with a GDC interlayer, Journal of Power Sources 160 (2006) 57–64.

[3] E. Perry Murray, M.J. Sever, S.A. Barnett, Electrochemical performance of LSCF–GDC composite cathodes, Solid State Ionics 148 (2002) 27–34.

[4] A. Petric, P. Huang, F. Tietz, Evaluation of La–Sr–Co–Fe–O perovskites for solid oxide fuel cells and gas separation membranes, Solid State Ionics 135 (2000) 719–725.

[5] G.C.H. Kostogloudis, C.H. Ftikos, Properties of A-site-deficient $La_{0.6}Sr_{0.4}Co_{0.2}Fe_{0.8}O_{3-\delta}$-based perovskite oxides, Solid State Ionics 126 (1999) 143–151.

[6] A.M. Amesti, A. Larrañaga, L.M.R. Martínez, Ma L. Nó, J.L. Pizarro, A. Laresgoiti, Ma I. Arriortua, Chemical compatibility between YSZ and SDC sintered at different atmospheres for SOFC applications, Journal of Power Sources 192 (2009) 151–157.

[7] A. Esquirol, N.P. Brandon, J.A. Kilner, M. Mogensen, Electrochemical characterization of $La_{0.6}Sr_{0.4}Co_{0.2}Fe_{0.8}O_3$ cathodes for intermediate-temperature SOFCs, Journal of the Electrochemical Society 151 (2004) A1847–A1855.

[8] H.Y. Tu, Y. Takeda, N. Imanishi, O. Yamamoto, $Ln_{0.4}Sr_{0.6}Co_{0.8}Fe_{0.2}O_{3-\delta}$ (Ln=La, Pr, Nd, Sm, Gd) for the electrode in solid oxide fuel cells, Solid State Ionics 117 (1999) 277–281.

[9] K.R. Reddy, K. Karan, Sinterability, mechanical, microstructural and electrical properties of gadolinium-doped ceria electrolyte for low-temperature solid oxide fuel cells, Journal of Electroceramics 15 (2005) 45–56.

[10] Y. Matsuzaki, I. Yasuda, Electrochemical properties of reduced-temperature SOFCs with mixed ionic–electronic conductors in electrodes and/or interlayers, Solid State Ionics 152-153 (2002) 463–468.

[11] Y. Leng, S.H. Chan, Q. Liu, Development of LSCF–GDC composite cathodes for low temperature solid oxide fuel cells with thin film GDC electrolyte, International Journal of Hydrogen Energy 33 (2008) 3808–3817.

[12] K. Sasaki, L.J. Gauckler, Functional gradient electrode/electrolyte for solid oxide fuel cells—gradient materials design for an electrochemical energy conversion device, in: Lausanne Ilschner (Ed.), Proceedings of the third International Symposium on Structurally and Functionally Graded Materials, Zürich, Switzerland, 1994, pp. 651–656.

[13] N.T. Hart, N.P. Brandon, M.J. Day, J.E. Shemilt, Functionally graded cathodes for solid oxide fuel cells, Journal of Materials Science 36 (2001) 1077–1085.

[14] S. Zha, Y. Zhang, M. Liu, Functionally graded cathodes fabricated by sol–gel/slurry coating for honeycomb SOFCs, Solid State Ionics 176 (2005) 25–31.

[15] P. Holtappels, C. Bagger, Fabrication and performance of advanced multi-layer SOFC cathodes, Journal of the European Ceramic Society 22 (2002) 41–48.

[16] S. Brunauer, P.H. Emmett, E. Teller, Adsorption of gases in multimolecular layers, Journal of the American Chemical Society 60 (1938) 309–319.

[17] R.A. Cutlera, D.L. Meixner, Ceria–lanthanum strontium manganite composites for use in oxygen generation systems, Solid State Ionics 159 (2003) 9–19.

[18] Y. Wang, K. Duncan, E.D. Wachsman, F. Ebrahimi, The effect of oxygen vacancy concentration on the elastic modulus of fluorite-structured oxides, Solid State Ionics 178 (2007) 53–58.
[19] Y.-S. Chou, J.W. Stevenson, T.R. Armstrong, L.R. Pedernson, Mechanical properties of $La_{1-x}Sr_xCo_{0.2}Fe_{0.8}O_3$ mixed-conducting perovskites made by the combustion synthesis technique, Journal of the American Ceramic Society 83 (2000) 1457–1464.
[20] A.C. Fischer-Cripps, in: Nanoindentation, second edition, Springer, New York, 2004.
[21] S. Guicciardi, T. Shimozono, G. Pezzotti, Nanoindentation characterization of sub-micrometric Y–TZP ceramics, Advanced Engineering Materials 8 (2006) 994–997.
[22] Shiwoo Lee, Sang Kuk Woo, Kee Sung Lee, Do Kyung Kim, Mechanical properties and structural stability of perovskite-type, oxygen-permeable, dense membranes, Desalination 193 (2006) 236–243.
[23] J.L. Shi, Relation between coarsening and densification in solid-state sintering of ceramics—experimental test on superfine zirconia powder compacts, Journal of Materials Research 14 (1999) 1389–1397.
[24] D. Music, U. Kreissig, Z.S. Czigány, U. Helmersson, J.M. Schneider, Elastic modulus–density relationship for amorphous boron suboxide thin films, Applied Physics A 76 (2003) 269–271.
[25] D. Music, U. Kreissig, V. Chirita, J.M. Schneider, Elastic modulus of amorphous boron suboxide thin films studied by theoretical and experimental methods, Journal of Applied Physics 93 (2003) 940–944.
[26] S.W. Kim, K.A.R. Khalil, High-frequency induction heat sintering of mechanically alloyed alumina–yttria-stabilized zirconia nano-bioceramics, Journal of the American Ceramic Society 89 (2006) 1280–1285.
[27] D. Chen, E.H. Jordan, M. Gell, X. Ma, Dense alumina–zirconia coatings using the solution precursor plasma spray process, Journal of the American Ceramic Society 91 (2008) 359–365.
[28] L.-W. Tai, M.M. Nasrallah, H.U. Anderson, D.M. Sparlin, S.R. Sehlin, Structure and electrical properties of $La_{1-x}Sr_xCo_{1-y}Fe_yO_3$. Part 1. The system $La_{0.8}Sr_{0.2}Co_{1-y}FeyO_3$, Solid State Ionics 76 (1995) 259–271.
[29] Y.-M. Yin, M.-W. Xiong, N.-T. Yang, Z. Tong, Y.-Q. Guo, Z.-F. Ma, E. Sun, J. Yamanis, B.-Y. Jing, Investigation on thermal, electrical, and electrochemical properties of scandium-doped $Pr_{0.6}Sr_{0.4}(Co_{0.2}Fe_{0.8})_{(1-x)}Sc_xO_{3-\delta}$ as cathode for IT-SOFC, International Journal of Hydrogen Energy 36 (2011) 3989–3996.
[30] H. Hayashi, M. Kanoh, C.J. Quan, H. Inaba, S. Wang, M. Dokiya, H. Tagawa, Thermal expansion of Gd-doped ceria and reduced ceria, Solid State Ionics 132 (2000) 227–233.
[31] L.-W. Tai, M.M. Nasrallah, H.U. Anderson, D.M. Sparlin, S.R. Sehlin, Structure and electrical properties of $La_{1-x}Sr_xCo_{1-y}Fe_yO_3$. Part 1. The system $La_{1-x}Sr_xCo_{0.2}Fe_{0.8}O_3$, Solid State Ionics 76 (1995) 273–283.
[32] S. Wang, M. Katsuki, M. Dokiya, T. Hashimoto, High temperature properties of $La_{0.6}Sr_{0.4}Co_{0.8}Fe_{0.2}O_{3-\delta}$ phase structure and electrical conductivity, Solid State Ionics 159 (2003) 71–78.
[33] A. Mineshige, J. Izutsu, M. Nakamura, K. Nigaki, J. Abe, M. Kobune, S. Fujii, T. Yazawa, Introduction of A-site deficiency into $La_{0.6}Sr_{0.4}Co_{0.2}Fe_{0.8}O_{3-\delta}$ and its effect on structure and conductivity, Solid State Ionics 176 (2005) 1145–1149.
[34] P. Zeng, R. Ran, Z. Chen, H. Gu, Z. Shao, J.C. Diniz da Costa, S. Liu, Significant effects of sintering temperature on the performance of $La_{0.6}Sr_{0.4}Co_{0.2}Fe_{0.8}O_{3-\delta}$ oxygen selective membranes, Journal of Membrane Science 302 (2007) 171–179.
[35] P. Ried, P. Holtappels, A. Wichser, A. Ulrich, T. Graule, Synthesis and characterization of $La_{0.6}Sr_{0.4}Co_{0.2}Fe_{0.8}O_{3-\delta}$ and $Ba_{0.5}Sr_{0.5}Co_{0.8}Fe_{0.2}O_{3-\delta}$, Journal of the Electrochemical Society 155 (2008) B1029–B1035.